

# JGR Solid Earth

## RESEARCH ARTICLE

10.1029/2020JB019356

### Key Points:

- Fault motion during the 2015 eruption of Axial Seamount contributed up to several centimeters of vertical motion to the deformation field
- Including estimates of fault-induced uplift results in a revised deformation source 2.1 km to the WSW from the previously modeled source
- Future source models should include fault motion to provide better estimates of active magma movement through time at Axial Seamount

### Supporting Information:

- Supporting Information S1

### Correspondence to:

W. L. Hefner,  
wh9516@uncw.edu

### Citation:

Hefner, W. L., Nooner, S. L., Chadwick, W. W., Jr, & Bohnenstiehl, D. W. R. (2020). Revised magmatic source models for the 2015 eruption at Axial Seamount including estimates of fault-induced deformation. *Journal of Geophysical Research: Solid Earth*, 125, e2020JB019356. <https://doi.org/10.1029/2020JB019356>

Received 6 JAN 2020

Accepted 22 MAR 2020

Accepted article online 24 MAR 2020

## Revised Magmatic Source Models for the 2015 Eruption at Axial Seamount Including Estimates of Fault-Induced Deformation

William L. Hefner<sup>1</sup> , Scott L. Nooner<sup>1</sup> , William W. Chadwick Jr<sup>2</sup> , and DelWayne R. Bohnenstiehl<sup>3</sup> 

<sup>1</sup>Department of Earth and Ocean Sciences, University of North Carolina Wilmington, Wilmington, NC, USA, <sup>2</sup>Hatfield Marine Science Center, Oregon State University/Cooperative Institute for Marine Resources Studies, Newport, OR, USA,

<sup>3</sup>Department of Marine, Earth, and Atmospheric Sciences and Center for Geospatial Analytics, North Carolina State University, Raleigh, NC, USA

**Abstract** Axial Seamount is an active submarine volcano located at the intersection of the Cobb hot spot and the Juan de Fuca Ridge (45°57'N, 130°01'W). Bottom pressure recorders captured co-eruption subsidence of 2.4–3.2 m in 1998, 2011, and 2015, and campaign-style pressure surveys every 1–2 years have provided a long-term time series of inter-eruption re-inflation. The 2015 eruption occurred shortly after the Ocean Observatories Initiative (OOI) Cabled Array came online providing real-time seismic and deformation observations for the first time. Nooner and Chadwick (2016, <https://doi.org/10.1126/science.aah4666>) used the available vertical deformation data to model the 2015 eruption deformation source as a steeply dipping prolate-spheroid, approximating a high-melt zone or conduit beneath the eastern caldera wall. More recently, Levy et al. (2018, <https://doi.org/10.1130/G39978.1>) used OOI seismic data to estimate dip-slip motion along a pair of outward-dipping caldera ring faults. This fault motion complicates the deformation field by contributing up to several centimeters of vertical seafloor motion. In this study, fault-induced surface deformation was calculated from the slip estimates of Levy et al. (2018, <https://doi.org/10.1130/G39978.1>) then removed from vertical deformation data prior to model inversions. Removing fault motion resulted in an improved model fit with a new best-fitting deformation source located 2.11 km S64°W of the source of Nooner and Chadwick (2016, <https://doi.org/10.1126/science.aah4666>) with similar geometry. This result shows that ring fault motion can have a significant impact on surface deformation, and future modeling efforts need to consider the contribution of fault motion when estimating the location and geometry of subsurface magma movement at Axial Seamount.

**Plain Language Summary** Axial Seamount is an active seafloor volcano located ~480 km west of the Oregon coast (45°57'N, 130°01'W) at the intersection of the Cobb hot spot and the Juan de Fuca Ridge. Frequent volcanism observed during eruptions in 1998, 2011, and 2015 make Axial Seamount an ideal location to study active magmatic processes using seafloor instrumentation. Leading up to the 2015 eruption the Ocean Observatories Initiative (OOI) Cable Array was brought online, providing real-time deformation and seismic observations over an eruption for the first time. Here we investigate the impact of fault motion along outward-dipping caldera faults estimated from the OOI seismic data on observed deformation for the 2015 eruption period. Including estimates of fault-induced deformation from 2015 eruption seismic data improved deformation/pressure source models originally derived by Nooner and Chadwick (2016, <https://doi.org/10.1126/science.aah4666>) and resulted in a new source location 2.11 km to the southwest. The results presented here suggest that fault motion impacts observed deformation at Axial Seamount and should be included in future modeling efforts.

## 1. Introduction

Axial Seamount is an active submarine volcano located ~480 km west of the Oregon coast (45°57'N, 130°01'W) at the intersection of the Cobb hot spot and the intermediate spreading rate (5–6 cm/yr) Juan de Fuca Ridge (JdFR). The summit caldera lies at a depth of ~1,500 m below sea level (bsl) and is a 3 × 8 km horseshoe-shaped depression with ~100-m high walls (Nooner & Chadwick, 2009; Figure 1). Rift zones extending to the north and south of the summit caldera accommodate dike propagation and magma intrusion from the summit reservoir during eruptions (Chadwick et al., 2016).

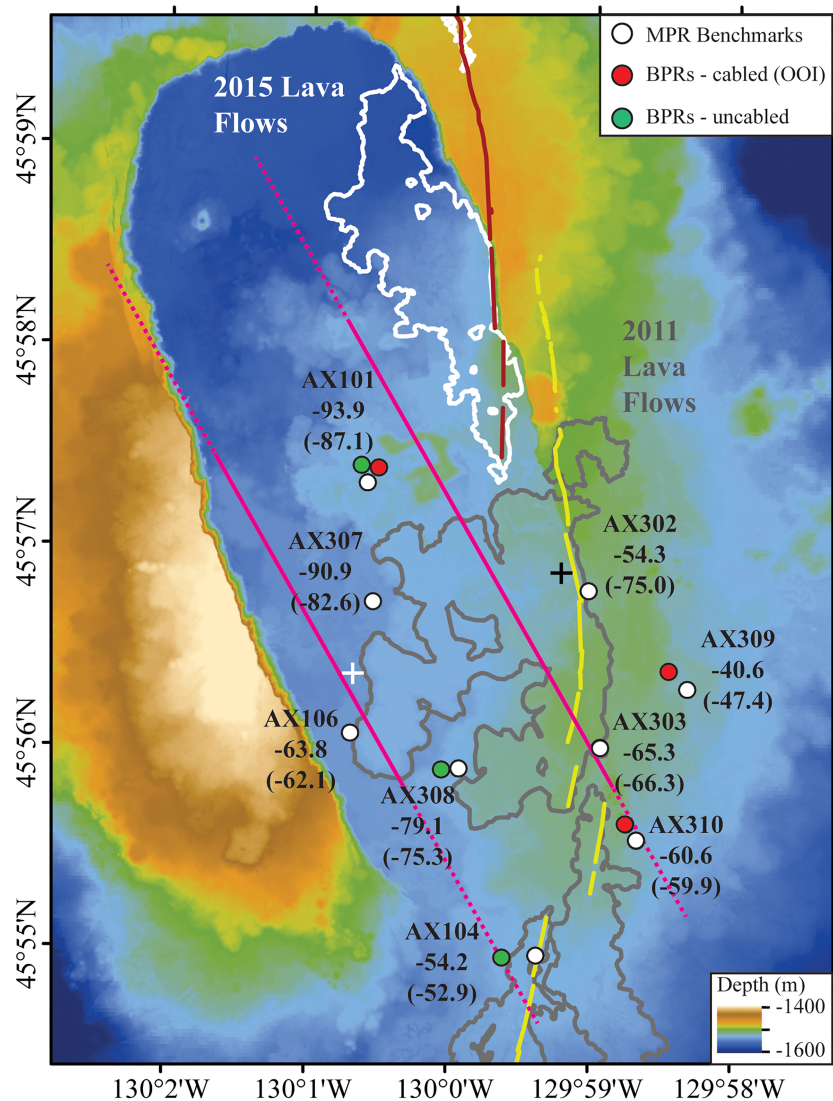


**Figure 1.** Map of Axial Seamount's summit caldera. MPR benchmarks (white circles) and BPRs (red and green circles) in place during the 2015 eruption. Pink lines indicate fault surface projections defined by seismically active outward-dipping fault planes inferred from OOI seismicity by Levy et al. (2018) with the solid portion representing 90% of moment release along strike. An additional reference benchmark 10 km to the south is not shown in this map view. Numbers indicate vertical deformation (cm) from MPR benchmarks between 14 September 2013 and 25 August 2015, and numbers in parentheses indicate vertical displacement with outward-dipping fault deformation estimates removed. Gray outlines and yellow lines indicate 2011 lava flows and fissures. White outlines and red lines indicate 2015 lava flows and fissures. The + symbol (black) is the centroid of the best-fit spheroidal deformation source to 2013–2015 MPR data from Nooner and Chadwick (2016). The + symbol (white) is the centroid of the revised 2015 spheroidal deformation source with fault deformation estimates removed from 2013–2015 MPR data.

Axial Seamount is one of the most intensively monitored submarine volcanoes in the world with three eruptions (1998, 2011, and 2015) observed since monitoring began in the 1990s (Caress et al., 2012; Chadwick et al., 2013; Chadwick et al., 2016; Fox et al., 2001). Estimates of the location, depth, and geometry of the underlying magma storage system from geodetic observations spanning these three eruptions indicate a depth of ~3–4 km to the centroid of deformation below the summit caldera (Chadwick et al., 2012; Fox et al., 2001; Nooner & Chadwick, 2016). West et al. (2001) used a 1999 seismic refraction study to image a summit magma chamber ~3 km below the seafloor, and results from a 2002 seismic reflection study indicate depths of 1.1–2.3 km to the top of the summit reservoir (Arnulf et al., 2014; Arnulf et al., 2018). Seismic data provide the most complete image of the subcaldera reservoir at one point in time, while long-term geodetic observations infer active magma movements for eruptions and inter-eruption periods.

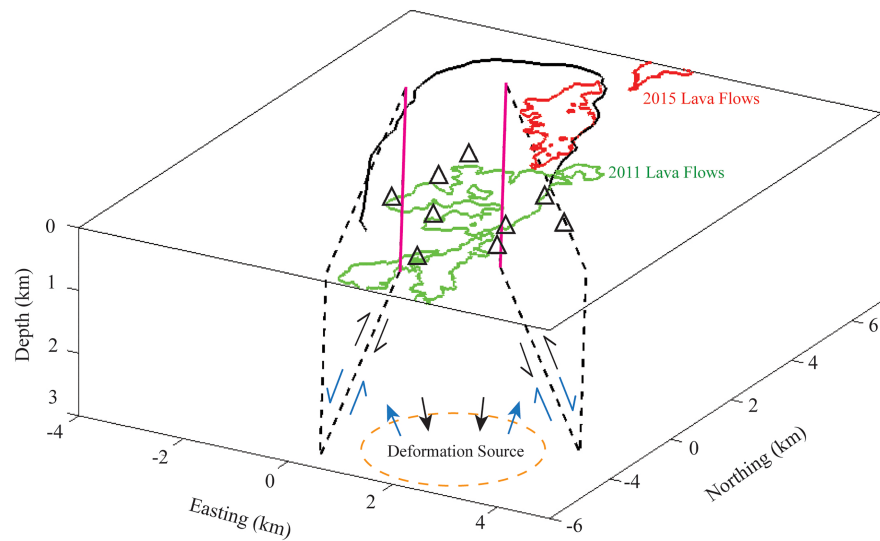


**Figure 2.** outward-dipping fault planes and MPR benchmarks. Three-dimensional view showing the location of outward-dipping fault planes (dashed black lines) and surface projections (magenta lines) fit to hypocenter locations determined by Levy et al. (2018) for the 2015 eruption period relative to MPR benchmarks (black triangles) inside Axial's summit caldera (black outline). The view is along strike of the seismically active fault planes at  $N30^{\circ}W$  dipping at angles of  $66^{\circ}E$  and  $66^{\circ}W$ , respectively. Normal fault motion accommodates volcanic inflation (blue arrows) of the summit reservoir (orange dashed line) leading up to the eruption. Fault motion is reversed during the eruption as diking emplaces magma along adjacent rift zones and the magma chamber (orange dashed line) starts to deflate (black arrows).

The 2015 eruption began on 24 April 2015 as a dike propagated up to  $\sim 14$  km from the caldera along the north rift zone and then erupted lava flows for 26 days (Chadwick et al., 2016; Clague et al., 2017; Wilcock et al., 2016; Wilcock, Dziak, et al., 2018). Nooner and Chadwick (2016) used bottom pressure data to model the best-fit deformation source for the 2015 eruption as a steeply dipping prolate-spheroid with a depth to center of 3.81 km located along the southeastern caldera wall (Figure 1). Seismic activity leading up to the 2015 eruption was captured by the Ocean Observatories Initiative (OOI) Cabled Array (Kelley et al., 2014) and was interpreted as the reactivation of two parallel outward-dipping faults below the western and eastern caldera walls, possibly parts of a larger ring fault system (Wilcock et al., 2016). With the OOI seismic network in place at Axial over 100,000 earthquakes were located during the 2015 eruption period (Wilcock, Dziak, et al., 2018). Fault motion along these faults produces a normal sense of slip during periods of inflation and a reverse sense of slip during co-eruption deflation (Levy et al., 2018; Wilcock et al., 2016; Figure 2). More recently, relocations of 2015 eruption hypocenters using improved velocity models indicate a set of conjugate outward and inward-dipping faults as parts of the ring fault system (Arnulf et al., 2018; Baillard et al., 2019).

At active volcanoes the source depth, geometry, and supply rate for the underlying magmatic system can be modeled based on geodetic observations of the rates and magnitudes of deformation at the surface (Dvorak & Dzuirsin, 1997). Deformation at active volcanoes is typically interpreted as the result of volume or pressure changes in the underlying reservoir; however, surface deformation patterns may also be impacted by displacements along active faults (Folch & Gottsmann, 2006). Although most of the vertical deformation at Axial Seamount appears to result from magma dynamics, caldera ring-fault motion could potentially generate enough surface motion to affect the deformation field of the volcano and, thus, also modeling results.

Levy et al. (2018) used the seismic data from the 2015 eruption to determine focal mechanisms on the faults identified by Wilcock et al. (2016) and to estimate dip-slip motion along the outward-dipping caldera faults (Figure 2). In this study, we model the surface deformation caused by this outward-dipping fault motion for the first time in order to assess the contribution that fault motion has on the observed seafloor deformation field and the implications for derived deformation source models for the 2015 eruption.

## 2. Methods and Results

### 2.1. Measuring Seafloor Deformation

Nearly continuous deformation monitoring at Axial Seamount since 1998 provides a long-term time series for constraining the timing, location, magnitude, and rates of vertical deformation associated with magma movement at depth. Vertical deformation at the volcano is measured with continuously recording bottom pressure recorders (BPRs) and campaign-style surveys at seafloor benchmarks using a mobile pressure recorder (MPR) during remotely operated vehicle (ROV) dives. Both methods precisely record overlying seawater pressure as a proxy for seafloor depth (Nooner & Chadwick, 2016). BPRs can detect vertical displacements of ~1 cm over short time scales (seconds to days) to document sudden events like eruptions (Chadwick et al., 2006). However, BPR sensor drift over longer time scales can obscure gradual or long-term deformation (Nooner & Chadwick, 2009; Polster et al., 2009).

MPR campaign-style surveys have been used since 2000 to measure long-term volcanic inflation at Axial Seamount. MPR surveys record seawater pressure on an array of seafloor benchmarks within the summit caldera relative to an assumed stable reference benchmark 10 km to the south (Chadwick et al., 2006; Figure 1). By making MPR measurements in a closed loop over a short time period (hours to days), short-term drift can be removed by repeat measurements. MPR surveys track gradual deformation over longer time periods (months to years) and can be used to correct for instrument drift in co-located BPRs (Chadwick et al., 2006; Nooner & Chadwick, 2009). Several alternative methods for constraining BPR drift are now being developed and evaluated (Sasagawa et al., 2016; Wilcock, Manalang, et al., 2018) but are not yet in routine widespread use.

MPR surveys were conducted on board the R/V *Thomas Thompson* in September 2013 and August 2015 using the ROV *Jason* to record pressure data at the 10 benchmarks in or near the summit caldera. BPRs (Figure 1) were also in place at five locations in the summit caldera during the same time period, but we use the MPR data to model the deformation source for the eruption because there are more measurement points.

### 2.2. Caldera ring-fault Slip Estimates

The OOI Cabled Array began providing seismic data from seven three-component ocean bottom seismometers (OBSs) in November 2014, with time-corrected data available after late January 2015, just 4 months before the eruption in April 2015 (Kelley et al., 2014; Wilcock et al., 2016). The cumulative distribution of dip-slip motion on the eastern and western ring faults was estimated from the OOI seismic data by Levy et al. (2018) for the pre-eruption, co-eruption, and post-eruption time periods from January 2015 to December 2016. Hypocenter distributions in cross section defined two outward-dipping bands of seismicity that approximate planes oriented ~N30°W/67°E (strike/dip) and ~N18°W/66°W, respectively (Levy et al., 2018).

For each microearthquake, we estimated its mean slip and area using a circular rupture model with a constant stress drop of 1 MPa and considering a range of shear moduli between 1 and 4 GPa (Gudmundsson et al., 2016). Here we represent the ring faults as two parallel-striking planes (N30°W) that dip outward from the caldera at 66°. Each fault was discretized as a  $0.25 \times 0.25$  m grid extending 3.25 km down-dip and 8 km along strike. The slip patch associated with each earthquake was projected orthogonally onto the nearest fault to its hypocenter. The final slip result for each time period was then smoothed using a Gaussian filter with a standard deviation (width) of 1 m. The cumulative motion along the eastern and western fault planes was determined by summing the slip from all the individual earthquakes during the pre-eruption and co-eruption time periods (Figure 3), under the assumption that fault motion is dominated by normal and reverse dip-slip motion during these respective time periods (Levy et al., 2018). Slip estimates from the post-eruption time period were not included because the moment release was extremely low and the amount of slip is assumed negligible (Levy et al., 2018; Wilcock et al., 2016; supporting information).

### 2.3. Deformation Source Modeling

We used the USGS package, dMODELS, from Battaglia et al. (2013) for both magma reservoir source inversions and forward models of fault-induced deformation from the cumulative caldera fault dip-slip estimates. Initial magma reservoir source inversions of 2013–2015 MPR data were determined by Nooner and

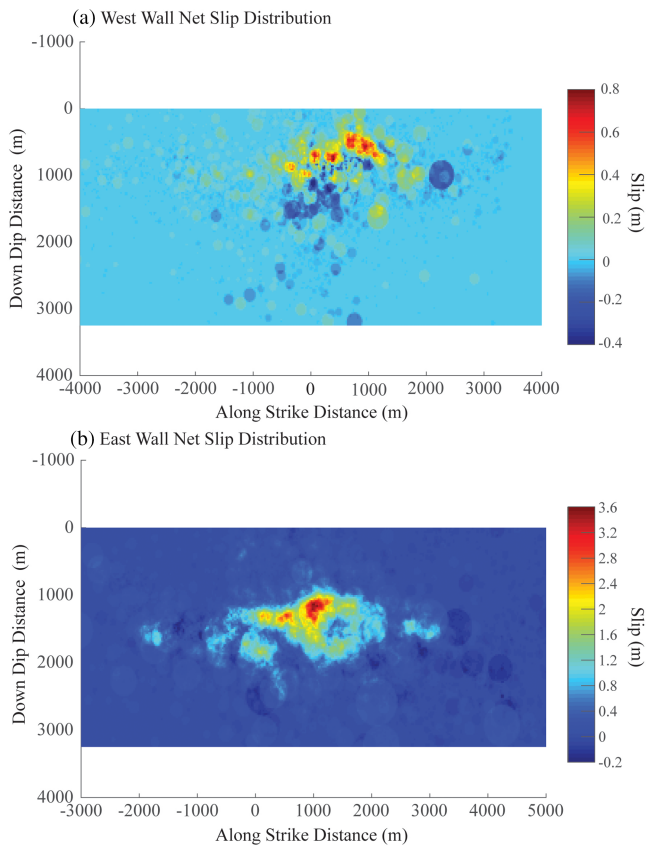


**Figure 3.** Cumulative 2015 eruption fault slip distributions. Net slip distributions gridded at  $5 \times 5$  m for the (a) western and (b) eastern faults for the periods of pre-eruption and co-eruption motion estimated from OOI seismic data assuming a shear modulus of 1 GPa. These net slip estimates include both normal slip during the pre-eruption period and reverse slip during the co-eruption period. Color bars indicate net slip in meters with negative slip values indicating the overall slip due to pre-eruption normal motion and positive slip values indicating the overall slip contributed by co-eruption reverse motion. Color scales differ between fault planes in order to highlight the low range of slip on the western fault.

Chadwick (2016) using the suite of inversion models in dMODELS consisting of spherical, prolate spheroid, and sill-like geometries (Fialko et al., 2001; McTigue, 1987; Yang et al., 1988). The best-fit source from each model inversion was determined using the reduced chi-square ( $\chi^2_{\text{reduced}}$ ) value. Nooner and Chadwick (2016) found the best-fitting deformation source ( $\chi^2_{\text{reduced}} = 34.2$ ) to the 2013–2015 MPR data to be a steeply dipping prolate-spheroid with major axis dipping  $77^\circ$  in the direction of  $286^\circ$ , with major and minor axes of 2.2 and 0.38 km, and located below the southeastern caldera wall at a depth of 3.81 km (Figures 1, 5, and 6). Nooner and Chadwick (2016) then used the prolate spheroid source parameters from the best-fit model to solve for the volume change due to the co-eruption subsidence recorded by five BPRs that were in place during the eruption (NSF Ocean Observatories Initiative Data Portal, 2016). They estimated the volume of magma removed from the summit reservoir at  $2.88 \times 10^8 \text{ m}^3$  which is 1.95 times the volume of lava erupted, implying that  $1.40 \times 10^8 \text{ m}^3$  of magma remained in the dike intrusion along the north rift zone (Chadwick et al., 2016).

Here, we update these calculations by first subtracting the vertical deformation caused by slip on the eastern and western caldera faults before re-running the source model inversions. While the pre-eruption normal slip estimates from January–April 2015 and the co-eruption reverse slip estimates from April–May 2015 do not entirely overlap with the 2013–2015 MPR observation time period, most of the fault motion occurred leading up to and during the 2015 eruption. While the 2013–2015 MPR data encompass a longer period of pre-eruption and post-eruption deformation, most of the cumulative seismic moment release from January 2015 to December 2016 occurred during the 26-day eruption period, with the co-eruptive reverse displacement on the faults being  $\sim 5.5$  times larger than the normal displacement observed in the preceding 3 months (Levy et al., 2018). The net cumulative dip-slip values for the eastern and western fault planes (Figure 3) were used to calculate surface deformation using the Okada (1992) solution for surface deformation from rectangular dislocations (approximating a fault) at depth. Here we model the estimated slip on each fault plane averaged over a  $1 \times 1$  m grid (a quarter of the original slip distribution grid at  $0.25 \times 0.25$  m), as the difference between model results at lower resolutions were negligible and the original resolution exceeded our available computing power at the time. We input the seismically derived slip for each  $1 \times 1$  m grid cell on the fault plane and calculated the net vertical deformation at the surface produced by all the  $1 \times 1$  m rectangular dislocations approximating net fault motion along each of the seismically defined outward-dipping fault planes for the 2015 eruption.

Since the amount of slip estimated from the seismic moment scales with the shear modulus, we first model the slip estimated assuming a shear modulus of 2 GPa and then double and half these slip estimates to allow for a 1–4 GPa range in the shear modulus appropriate for basaltic rock (Gudmundsson et al., 2016; supporting information and Figure 3). Estimates of surface deformation were determined from both the eastern and western fault planes, but the slip on the eastern fault dominates fault-induced deformation, due to the much higher rates of seismicity along the eastern fault (Figure 4). Recent results by Moyer et al. (2017) suggest that the ring faults may be stronger than assumed here, with average stress drops of 3–6 MPa. Higher stress drop would imply more compact (smaller radius) ruptures; however, since the scale of these potential irregularities is small compared to their depths, the assumed stress drop has negligible impact on the vertical seafloor deformation field (Pollard et al., 1983). Estimates of fault-induced vertical deformation for the range of possible shear moduli at the MPR benchmark locations (Table 1) were then removed from the MPR data set prior to running the sphere, prolate spheroid, and sill-like source inversions in dMODELS (Fialko et al., 2001; McTigue, 1987; Yang et al., 1988; supporting information).

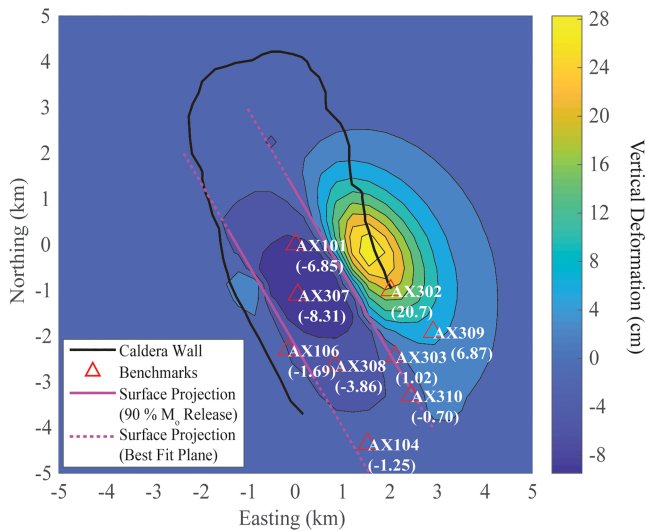


**Figure 4.** Modeled fault-induced deformation. Net surface deformation pattern estimated from 2015 eruption cumulative dip-slip motion for the pre-eruption and co-eruption time periods from the earthquake catalog of Levy et al. (2018) assuming a shear modulus of 1 GPa. outward-dipping caldera ring fault planes are oriented N30°W dipping 66°E and 66°W, respectively. Positive vertical deformation values indicate uplift, and negative values indicate subsidence. Numbers in parentheses indicate vertical deformation (cm) estimates for each benchmark.

The best-fitting deformation source ( $\chi^2_{\text{reduced}} = 15.2$ ) for the 2013–2015 MPR data with the modeled deformation from fault motion removed is still a steeply dipping prolate-spheroid but is located 2,110 m S64°W of the best-fit source from Nooner and Chadwick (2016) (supporting information). This best-fit model is based on slip values estimated assuming a shear modulus of 1 GPa (which maximized the contribution from fault slip) and has a major axis dipping 86° in the direction of 012°, with major and minor axes of 1.7 and 0.36 km located along the southwestern caldera wall at a depth of 3.01 km (Figures 1, 5, and 6). As stated above, this inversion includes a period of pre-eruption inflation, co-eruption deflation, and post-eruption inflation from 2013–2015 MPR data but with the removal of fault displacement estimates for a shorter time period of pre-eruption and co-eruption deformation from January to May 2015. Using the newly revised best-fit spheroid source parameters and co-eruption fault deformation estimates using a shear modulus of 1 GPa, we calculate the volume of magma removed from the summit reservoir during co-eruption subsidence in 2015 to be  $2.06 \times 10^8 \text{ m}^3$  (supporting information; Segall, 2013) compared to  $2.88 \times 10^8 \text{ m}^3$  calculated by Nooner and Chadwick (2016) without considering fault motion.

### 3. Discussion

Including deformation due to dip-slip fault motion estimated from 2015 eruption-related seismicity improved the model fit to 2013–2015 MPR data reducing the  $\chi^2_{\text{reduced}}$  value from 34.2 to 15.2 as well as the  $\sigma_{\text{residuals}}$  from 0.069 to 0.044 m (Figure 5). Improved model fit suggests that motion on outward-dipping faults contributed a significant amount to the surface deformation observed over the 2015 eruption period. Estimates of fault-induced deformation at the MPR benchmarks (Table 1) make clear the potential importance of including fault motion in deformation models at Axial Seamount. For example, MPR benchmark AX302 had the maximum estimated vertical deformation due to fault dip-slip motion for the range of shear moduli at 0.052–0.207 m amounting to ~8–38% of the observed vertical displacements there (−0.543 m to [−0.595 to −0.750] m). These estimates suggest that a significant percentage of magma-induced subsidence at AX302 is obscured by net vertical motion of the caldera rim due to fault displacement.

The maximum estimated vertical deformation due to fault motion over the model domain (Figure 4) is ~0.7–0.28 m (estimated using the range of possible shear moduli) located east of the eastern fault plane. Cumulative fault motion along the eastern and western faults produced uplift east and west of the caldera and subsidence in the caldera center. Liu et al. (2019) investigated the impact of ring faulting on surface deformation during caldera subsidence through both analog experiments and boundary element modeling. They proposed that broad deformation patterns observed at active volcanic centers are the result of volume change within the magma reservoir, while localized intra-caldera subsidence is the result of motion along reactivated ring faults at depth. Our fault-derived deformation estimates for the model domain produced a similar pattern of focused co-eruption subsidence at the caldera center. However, net slip along the eastern fault was significantly greater than the western fault (Figures 3 and 4), and the eastern fault contributed most of the fault-derived surface deformation (Figure 4). The dominant reverse sense of slip on the eastern fault for the 2015 co-eruption period resulted in increased subsidence recorded at MPR benchmarks within the caldera between the east and west caldera faults as the hanging wall moved upward relative to the footwall (Figures 2 and 4).

The best-fitting deformation source for the 2015 eruption from Nooner and Chadwick (2016) was a steeply dipping spheroid with a depth to center of 3.81 km located along the southeastern caldera wall (Figures 1, 5, and 6). They interpreted their best-fitting spheroid location as a nearly vertical conduit that feeds the high-melt core of the large magma reservoir imaged by Arnulf et al. (2014). However, removing fault deformation estimates from the MPR data before running model inversions results in a new source location 2.11 km to the southwest (Figures 1, 5, and 6). This is because the eastern caldera fault had the most slip

**Table 1**  
Observed Uplift From 2013–2015 MPR Data and Fault-Induced Deformation Estimates for the Range of Possible Shear Moduli for Fractured Basalt From 1–4 GPa

Benchmark	MPR observed uplift (m)	Predicted seafloor uplift from faulting (m)		
		$\mu = 1$ GPa	$\mu = 2$ GPa	$\mu = 4$ GPa
AX101	-0.9390	-0.0685	-0.0342	-0.0171
AX106	-0.6380	-0.0169	-0.0084	-0.0042
AX104	-0.5418	-0.0125	-0.0063	-0.0031
AX105	0.0000	-0.0008	-0.0004	-0.0002
AX302	-0.5431	0.2065	0.1032	0.0516
AX303	-0.6532	0.0102	0.0051	0.0026
AX307	-0.9093	-0.0831	-0.0415	-0.0208
AX308	-0.7911	-0.0386	-0.0193	-0.0097
AX309	-0.4057	0.0687	0.0343	0.0172
AX310	-0.6056	-0.0070	-0.0035	-0.0017

during the eruption and that slip produced relative uplift on the eastern side of the caldera, which pulls the model inversions that ignore faulting to the east. It is important to note that deformation source models do not necessarily reflect the exact geometry of the magma reservoir at depth but rather relate observed surface deformation to the location of the greatest volume/pressure change at depth approximated by simplified geometries (sphere, spheroid, and sill).

The new best-fitting model to the 2013–2015 MPR data with faulting included has a source depth of 3.01 km compared to 3.81 km from Nooner and Chadwick (2016). These source depths both generally agree with multichannel seismic (MCS) survey results and geochemical analysis that indicate a crustal summit reservoir centered at ~2–4 km below the caldera (Arnulf et al., 2014; Dreyer et al., 2013; West et al., 2001). They are also both within the outline of the summit magma reservoir imaged by Arnulf et al. (2014, 2018).

In this study we modeled 2015 eruption fault motion as two parallel outward-dipping planes. However, recent work by Arnulf et al. (2018) and Baillard et al. (2019) placed 2015 eruption hypocenter locations along conjugate inward and outward-dipping faults as part of the larger ring fault system underlying Axial. Arnulf et al. (2018) used an improved 3-D velocity structure from 2002 MCS data to relocate 2015 eruption hypocenters resulting in shallower outward-dipping bands with dips

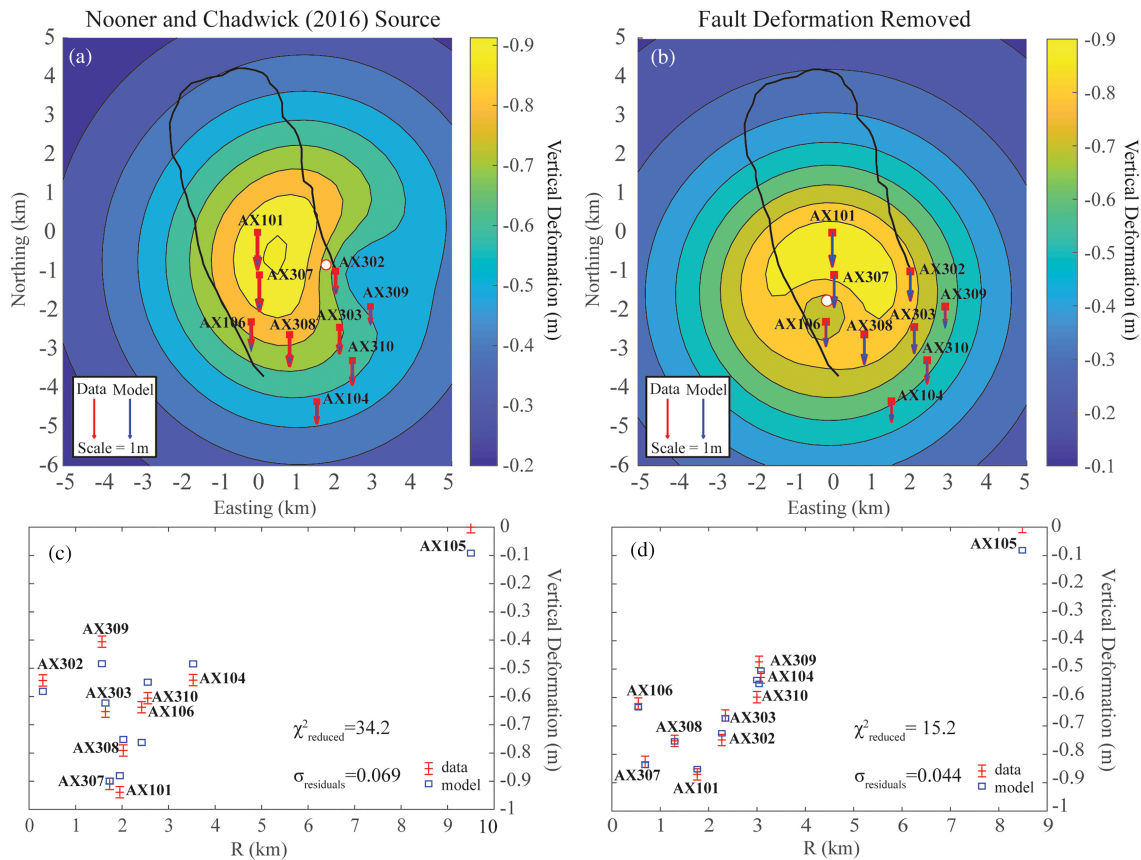


**Figure 5.** Deformation modeling results. (a) Map view of vertical displacement from the best-fit spheroidal source geometry to 2013–2015 MPR data from Nooner and Chadwick (2016) (centroid indicated by white circle). (b) Map view of vertical displacement from the best-fit spheroidal source to 2013–2015 MPR data with estimated fault-induced deformation from net fault motion for the 2015 eruption period removed (centroid indicated by white circle). (c) and (d) Error plots for each of the respective best-fit sources above showing observed (red error bars) and modeled (blue boxes) results at each benchmark compared to the radial distance from the centroid of the best-fit source.

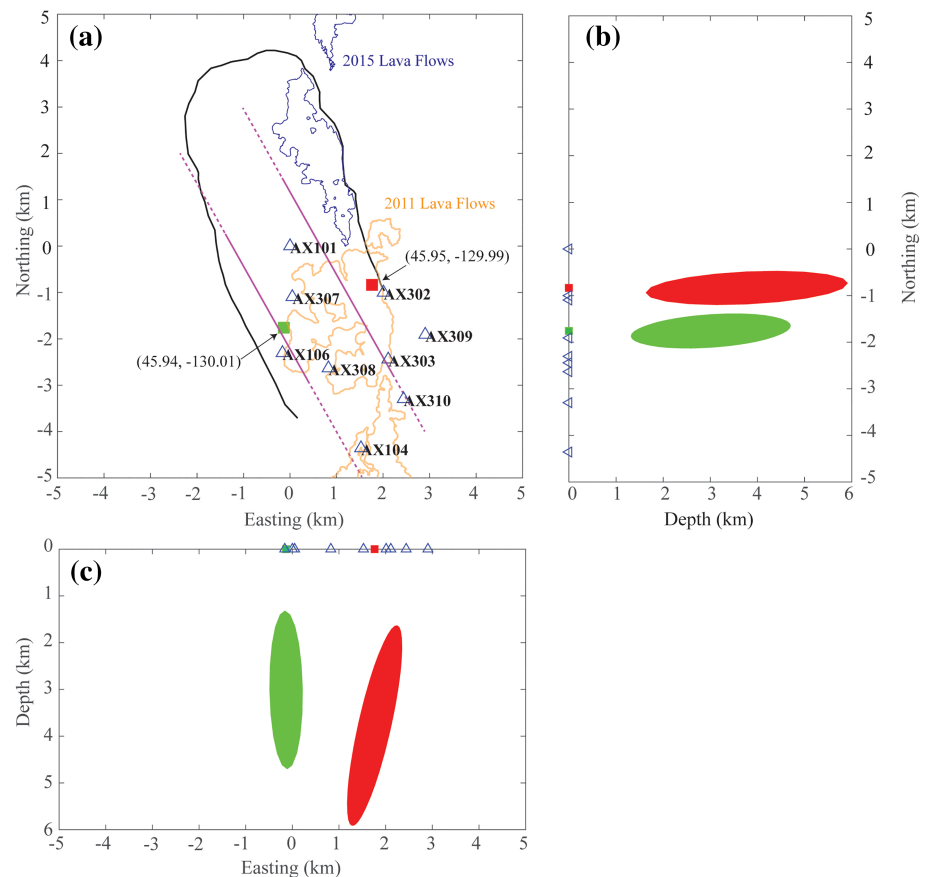


**Figure 6.** Deformation source 3-D geometry. (a) Caldera rim with MPR benchmarks as blue triangles showing the best-fit deformation source locations to 2013–2015 MPR data with and without 2015 eruption fault-induced deformation removed. Y-axis is aligned north-south with no coordinate rotation. The red square is the centroid of the source result without net fault-induced deformation removed. The green square is the centroid of the source result with net fault-induced deformation removed. Latitude/longitude in decimal degrees of each centroid is shown in parentheses. Surface projections of seismically defined outward-dipping fault planes are shown in magenta with the solid line representing 90% moment release along strike. (b) North-south and (c) east-west depth profiles of the best-fit spheroids to MPR data (red) and MPR data with fault motion removed (green).

of  $42^\circ$  to  $60^\circ$  compared to our modeled fault planes at  $66^\circ$  as well as a set of conjugate inward-dipping faults beneath the northern caldera. Because fault depth, strike, and inclination all impact modeled surface displacement from fault dislocations at depth, we modeled our original fault planes at dips of  $42^\circ$ ,  $50^\circ$ , and  $60^\circ$  and removed these estimates prior to running a spheroidal source inversion again. Removing fault deformation estimates over this range of dip values resulted in similar source locations west of the source of Nooner and Chadwick (2016) and decreased the model fit (supporting information). However, the effects of slip on inward-dipping conjugate faults on the surface deformation were not investigated as slip estimates have not been calculated on them.

New analysis of seismic data from the Juan de Fuca Ridge and Axial Seamount has revealed the presence of deeper reflections interpreted as magma sills beneath the previously imaged axial magma lens (AML) (Carbotte et al., 2018; Carbotte et al., 2019). The deeper reflections are interpreted as vertically stacked melt lenses extending to depths of 6 km beneath the southern portion of the caldera over a 3–5 km wide region and suggest a vertical conduit. This conduit is consistent with the geometry and depth extent to the deformation source of Nooner and Chadwick (2016) as well as the new model results presented in this paper. However, while the source of Nooner and Chadwick (2016) is located just outside the extent of the 3–5 km wide, deep melt mush conduit of Carbotte et al. (2019), our revised deformation source location is located within its extent, so it is perhaps in better agreement. The vertically stacked melt lenses also

underlie the melt-rich part of the shallow summit reservoir interpreted as the source of the 1998, 2011, and 2015 eruptions and dike intrusions (Carbotte et al., 2019). Despite some differences in details, these independent lines of geophysical evidence (deformation modeling with and without considering faulting, and multichannel seismic imaging of both the shallow and deep crust) all agree that the core of the high-melt magma supply and storage system at Axial Seamount is beneath the southern part of the summit caldera.

#### 4. Conclusions

The new modeling results presented here build on the previous deformation source models presented by Nooner and Chadwick (2016) for the 2015 eruption prior to caldera-fault slip estimates from Levy et al. (2018). This study considers what effect caldera fault motion has on the modeling of the 2015 eruption deformation source of Nooner and Chadwick (2016) through the inclusion of caldera fault motion in the inversion 2013–2015 MPR data. The best-fitting deformation source for the 2015 eruption including estimates of caldera fault motion is a steeply dipping prolate-spheroid located 2.11 km S64°W of the source of Nooner and Chadwick (2016) at a depth of 3.01 km (Figures 1, 5, and 6). In addition to the revised location of the deformation source with fault-induced deformation removed, we provide an updated estimate of the volume change during co-eruption subsidence with co-eruption fault deformation removed at  $2.06 \times 10^8 \text{ m}^3$  which is ~28% less than previous estimates calculated by Nooner and Chadwick (2016) at  $2.88 \times 10^8 \text{ m}^3$  (supporting information).

While including fault-derived deformation resulted in improved model fit, constraining fault geometry and slip magnitudes from the 2015 seismic data is complicated by the temporal mismatch of data sets and uncertainty in the shear modulus and crustal structure at Axial Seamount. While the fault-derived deformation presented here does not entirely match the same time period as our MPR data set, we assume that the co-eruption period accounts for the bulk of fault motion over the 2015 eruption. However, seismic observations over the next entire eruption cycle will allow us to better determine the amount of slip during each phase of the eruption further constraining fault-derived deformation estimates for benchmark deformation data. While we investigated the effect of different outward-dipping fault inclinations on model results, motion on the conjugate inward-dipping faults recently identified by Arnulf et al. (2018) could also alter our fault-derived deformation estimates. We also cannot rule out the possibility of aseismic slip along either set of faults—particularly during the early post-eruption period when uplift rates rival those observed immediately pre-eruption; yet, there are few earthquakes observed. With a 3-D seismic survey on the R/V *Marcus Langseth* in summer 2019, there is the potential to improve fault motion estimates for the next eruption along more complex fault structures. Three-dimensional seismic data will improve our understanding of the 3-D structure of Axial Seamount's summit reservoir, complex ring faults, and magma conduits allowing us to further constrain fault models and the interpretations from deformation source model results presented here.

Following the 2015 eruption the number of continuously recording BPRs was expanded with the deployment of small, uncabled BPRs on or near all the MPR benchmarks. Expanding the number of BPRs will provide better constraints on rapid deformation events during the next eruption at Axial Seamount as well as provide the potential to track short-term deformation events between repeat MPR surveys. The combination of expanded deformation coverage along with estimates of fault motion from seismicity data will provide a more complete picture of active magma dynamics over subsequent eruption cycles at Axial Seamount. With the current rate of volcanic inflation at Axial Seamount, the volcano is expected to reach 2015 pre-eruption inflation levels by the early-2020s ([https://www.pmel.noaa.gov/eoi/axial\\_blog.html](https://www.pmel.noaa.gov/eoi/axial_blog.html)). The next eruption at Axial Seamount will provide the first opportunity to combine expanded data coverage with high-precision instruments and potential observations of caldera fault seismicity in the same deformation source model inversion providing an even better constrained solution from geodetic observations for the deformation source related to the active reservoir at depth. The results of improved model fit from the inclusion of 2015 eruption ring-fault seismic data indicate that fault motion over all phases of the eruption cycle impacts observed deformation and that future geodetic source models should include fault motion to provide better estimates of active magma movement through time at Axial Seamount.

**Acknowledgments**

The BPR data presented here are archived at the Integrated Earth Data Applications Marine Geoscience Data System (Chadwick & Nooner, 2018). Pressure and seismic data from the OOI Cabled Array are available on the National Science Foundation Ocean Observatories Initiative Data Portal (<https://oceanobservatories.org/data-portal/>) OOI Data Portal, and earthquake data from Levy et al. (2018) are available at the IRIS Data Management Center (<https://ds.iris.edu/ds/nodes/dmc/>). This work was supported by NSF Awards OCE-1356216 and 1546616 and by the National Oceanic and Atmospheric Administration, Pacific Marine Environmental Laboratory (NOAA-PMEL). We also thank the crews of the R/V *Thomas Thompson* and ROV *Jason* for support and data acquisition at sea. This work was made possible thanks to the support of the NOAA-PMEL Engineering Division and the University of Washington OOI Cabled Array team, led by J. Delaney and D. Kelley.

**References**

Arnulf, A. F., Harding, A., Kent, G., Carbotte, S., Canales, J. P., & Nedimovic, M. (2014). Anatomy of an active submarine volcano. *Geology*, *42*(8), 655–658. <https://doi.org/10.1130/G35629.1>

Arnulf, A. F., Harding, A. J., Kent, G. M., & Wilcock, W. S. D. (2018). Structure, seismicity, and accretionary processes at the hot spot-influenced Axial Seamount on the Juan de Fuca Ridge. *Journal of Geophysical Research: Solid Earth*, *123*, 1–29. <https://doi.org/10.1029/2017JB015131>

Baillard, C., Wilcock, W. S. D., Arnulf, A. F., Tolstoy, M., & Waldhauser, F. (2019). A joint inversion for three-dimensional *P* and *S* wave velocity structure and earthquake locations beneath Axial Seamount. *Journal of Geophysical Research: Solid Earth*, *124*, 12,997–13,020. <https://doi.org/10.1029/2019JB017970>

Battaglia, M., Cervelli, P. F., & Murray, J. R. (2013). Modeling crustal deformation near active faults and volcanic centers—A catalog of deformation models. *U.S. Geological Survey Techniques and Methods*, book 13, chap. B1, 1–96. <https://pubs.usgs.gov/tm/13/b1>.

Carbotte, S. M., Arnulf, A. F., Spiegelman, M. W., Lee, M., Harding, A. J., Kent, G. M., et al. (2019). Seismic images of a deep melt-mush feeder conduit beneath Axial Volcano. Abstract OS51B-1484 presented at 2019 fall AGU meeting, San Francisco, CA, 10–14 Dec.

Carbotte, S. M., Canales, J. P., Marjanovic, M., & Nedimovic, M. R. (2018). New seismic observations of multi-level magma sills beneath the axis of the Juan de Fuca Ridge. Abstract V43G-0210 presented at 2018 fall AGU meeting, Washington, D.C., 10–14 Dec.

Caress, D. W., Clague, D. A., Paduan, J. B., Martin, J., Dreyer, B., Chadwick, W. W. Jr., et al. (2012). Repeat bathymetric surveys at 1-metre resolution of lava flows erupted at Axial Seamount in April 2011. *Nature Geoscience*, *5*(7), 483–488. <https://doi.org/10.1038/NGEO1496>

Chadwick, W. W. Jr., Clague, D. A., Embley, R. W., Perfit, M. R., Butterfield, D. A., Caress, D. W., et al. (2013). The 1998 eruption of Axial Seamount: New insights on submarine lava flow emplacement from high-resolution mapping. *Geochemistry, Geophysics, and Geosystems*, *14*(10), 3939–3968. <https://doi.org/10.1002/ggge20202>

Chadwick, W. W., Jr., & Nooner, S. L. (2018). Processed bottom pressure recorder (BPR) data from uncabled instruments deployed at Axial Seamount on the Juan de Fuca Ridge (investigators William Chadwick and Scott Nooner). *Integrated Earth Data Applications (IEDA)*, <http://get.iedadata.org/doi/322282>.

Chadwick, W. W. Jr., Nooner, S. L., Butterfield, D. A., & Lilley, M. D. (2012). Seafloor deformation and forecasts of the April 2011 eruption at Axial Seamount. *Nature Geoscience*, *5*(7), 474–477. <https://doi.org/10.1038/NGEO1464>

Chadwick, W. W. Jr., Nooner, S. L., Zumberge, M. A., Embley, R. W., & Fox, C. G. (2006). Vertical deformation monitoring at Axial Seamount since its 1998 eruption using deep-sea pressure sensors. *Journal of Volcanology and Geothermal Research*, *150*, 313–327. <https://doi.org/10.1016/j.jvolgeores.2005.07.006>

Chadwick, W. W. Jr., Paduan, J. B., Clague, D. A., Dreyer, B. M., Merle, S. G., Bobbitt, A. M., et al. (2016). Voluminous eruption from a zoned magma body after an increase in supply rate at Axial Seamount. *Geophysical Research Letters*, *43*, 12,063–12,070. <https://doi.org/10.1002/2016GL071327>

Clague, D. A., Paduan, J. B., Caress, D. W., Chadwick, W. W. Jr., Saout, M. L., Dreyer, B., & Portner, R. (2017). High-resolution AUV mapping and targeted ROV observations of three historical lava flows at Axial Seamount. *Oceanography*, *30*, 82–99. <https://doi.org/10.5670/oceanog.2017.426>

Dreyer, B. M., Clague, D. A., & Gill, J. B. (2013). Petrologic variability of recent magmatism at Axial Seamount summit, Juan de Fuca Ridge. *Geochemistry, Geophysics, Geosystems*, *14*, 4306–4333. <https://doi.org/10.1002/ggge.20239>

Dvorak, J. J., & Dzuirsin, D. (1997). Volcano geodesy: The search for magma reservoirs and the formation of eruptive vents. *Reviews of Geophysics*, *35*, 343–384.

Fialko, Y., Khazan, Y., & Simons, M. (2001). Deformation due to a pressurized horizontal circular crack in an elastic half-space, with applications to volcano geodesy. *Geophysics Journal International*, *146*, 181–190.

Folch, A., & Gottsmann, J. (2006). Faults and ground uplift at active calderas. *The Geological Society of London*, *269*, 109–120.

Fox, C. G., Chadwick, W. W. Jr., & Embley, W. E. (2001). Direct observation of a submarine volcanic eruption from a sea-floor instrument caught in a lava flow. *Nature*, *412*(6848), 727–729. <https://doi.org/10.1038/35089066>

Gudmundsson, M. T., Jónsdóttir, K., Hooper, A., Holohan, E. P., Halldórsson, S. A., Ófeigsson, B. G., et al. (2016). Gradual caldera collapse at Bárðarbunga volcano, Iceland, regulated by lateral magma outflow. *Science*, *353*, 1–24. <https://doi.org/10.1126/science.aaf8988>

Kelley, D. S., Delaney, J. R., & Juniper, S. K. (2014). Establishing a new era of submarine volcanic observations: Cabling Axial Seamount and the Endeavour Segment of Juan de Fuca Ridge. *Marine Geology*, *352*, 426–450. <https://doi.org/10.1016/j.margeo.2014.03.010>

Levy, S., Bohnenstiehl, D. R., Sprinkle, P., Boettcher, M. S., Wilcock, W. S. D., Tolstoy, M., & Waldhauser, F. (2018). Mechanics of fault reactivation before, during, and after the 2015 eruption of Axial Seamount. *Geology*, *46*, 447–450. <https://doi.org/10.1130/G39978.1>

Liu, Y.-K., Ruch, J., Vasyura-Bathke, H., & Jónsson, S. (2019). Influence of ring faulting in localizing surface deformation at subsiding calderas. *Earth and Planetary Science Letters*, *526*, 377–378. <https://doi.org/10.1016/j.epsl.2019.115784>

McTigue, D. F. (1987). Elastic stress and deformation near a finite spherical magma body: Resolution of the point source paradox. *Journal of Geophysical Research*, *92*(B12), 12,931–12,940.

Moyer, P. A., Boettcher, M. S., & Bohnenstiehl, D. R. (2017). Earthquake stress drop before, during, and after the 2015 eruption at Axial Seamount. Abstract 203092 presented at 2017 AGU Chapman conference, Hobart, Tasmania, Australia, 29 Jan.-3 Feb.

Nooner, S. L., & Chadwick, W. W. Jr. (2009). Volcanic inflation measured in the caldera of Axial Seamount: Implications for magma supply and future eruptions. *Geochemistry Geophysics Geosystems*, *10*, 1–14. <https://doi.org/10.1029/2008GC002315>

Nooner, S. L., & Chadwick, W. W. Jr. (2016). Inflation-predictable behavior and co-eruption deformation at Axial Seamount. *Science*, *354*(6318), 1399–1403. <https://doi.org/10.1126/science.aah4666>

NSF Ocean Observatories Initiative, Data portal, bottom pressure tilt (RS03CCAL-MJ03F-BOTPTA301, RS03ECALMJ03E-BOTPTA302, RS03INT2-MJ03D-BOTPTA303), data from 16 September 2014 to 20 May 2016; <http://ooinet.oceanobservatories.org>.

Okada, Y. (1992). Internal deformation due to shear and tensile faults in a half-space. *Bulletin of the Seismological Society of America*, *82*(2), 1018–1040.

Pollard, D. D., Delaney, P. T., Duffield, W. A., Endo, E. T., & Okamura, A. T. (1983). Surface deformation in volcanic rift zones. *Tectonophysics*, *94*, 541–584.

Polster, A., Fabian, M., & Villinger, H. (2009). Effective resolution and drift of Paroscientific pressure sensors derived from long-term seafloor measurements. *Geochemistry Geophysics Geosystems*, *10*(8), 1–9. <https://doi.org/10.1029/2009GC002532>

Sasagawa, G. S., Cook, M. J., & Zumberge, M. A. (2016). Drift-corrected seafloor pressure observations of vertical deformation at Axial Seamount 2013–2014. *Earth and Space Science*, *3*, 381–385. <https://doi.org/10.1002/2016EA000190>

Segall, P. (2013). Volcano deformation and eruption forecasting. *Geological Society of London Special Publication*, *380*, 85–106. <https://doi.org/10.1144/SP380.4>

- West, M., Menke, W., Tolstoy, M., Webb, S., & Sohn, R. (2001). Magma storage beneath Axial volcano on the Juan de Fuca mid-ocean ridge. *Nature*, *413*(6858), 833–836. <https://doi.org/10.1038/35101581>
- Wilcock, W. S. D., Dziak, R. P., Tolstoy, M., Chadwick, W. W. Jr., Nooner, S. L., Bohnenstiehl, D. R., et al. (2018). The recent volcanic history of Axial Seamount: Geophysical insights into past eruption dynamics with an eye toward enhanced observations of future eruptions. *Oceanography*, *31*(1), 114–123. <https://doi.org/10.5670/oceanog.2018.117>
- Wilcock, W. S. D., Manalang, D., Harrington, M., Cram, G., Fredrickson, E. K., Tilley, J., et al. (2018). Self-calibrating resonant quartz crystal technology sensors for seafloor geodesy and oceanographic applications. Abstract OC21E-1615 presented at 2018 Fall AGU Meeting, Washington, DC, 10–14 Dec.
- Wilcock, W. S. D., Tolstoy, M., Waldhauser, F., Garcia, C., Tan, Y. J., Bohnenstiehl, D. R., et al. (2016). Seismic constraints on caldera dynamics from the 2015 Axial Seamount eruption. *Science*, *354*(6318), 1395–1399. <https://doi.org/10.1126/science.aah556>
- Yang, X., Davis, P. M., & Dieterich, J. H. (1988). Deformation from inflation of a dipping finite prolate spheroid in an elastic half-space as a model for volcanic stressing. *Journal of Geophysical Research: Solid Earth*, *93*, 4249–4257. <https://doi.org/10.1029/JB093iB05p04249>